

# Condition Monitoring for Flight Performance Estimation of Small Multirotor Unmanned Aerial Vehicles

Daniel Wolfram, Florian Vogel, Dominik Stauder  
Institute of Flight Systems and Automatic Control  
Technische Universität Darmstadt  
Otto-Berndt-Str. 2  
64287 Darmstadt, Germany  
wolfram@fsr.tu-darmstadt.de

**Abstract**— This study deals with a condition-based determination of small multirotor Unmanned Aerial Vehicles (UAV) flight performance. Knowledge of the actual flight performance enables an evaluation of mission risk for adaptive mission planners and an optimization of parameters for adaptive flight controllers. At the beginning of this paper basic principles of multicopter's flight mechanics are presented on the design of a X8 multicopter. The platform is designed as a quadcopter with redundant drives in coaxial configuration at each arm. The multicopter's flight performance is primarily influenced by its drive trains. A conventional drive train consists of accumulator, electronic speed controller, brushless direct current motor and propeller. Performance losses caused by faults or degradation of one of these components, directly affect the performance and safety of the entire multirotor UAV. This paper introduces a Condition Monitoring (CM) system, which examines the input and output power of the drive train's individual components by analyzing suitable sensor data. One important objective is the detection, isolation and identification of selected faults, which influence the power of the drive train. A test rig was developed to provide real data to investigate the fault behavior under laboratory conditions. Algorithms for sensor based flight performance estimation are first tested in a complex simulation environment. It consists of several modules, such as a model of the drive train with the possibility of simulating fault states, as well as a model of the complete research copter platform. Finally, the influence of technical faults on the multicopter's flight performance is presented.

## TABLE OF CONTENTS

<b>1. INTRODUCTION</b> .....	<b>1</b>
<b>2. FLIGHT PERFORMANCE ANALYSIS WITH A X8 TEST SYSTEM</b> .....	<b>2</b>
<b>3. COMPONENTS OF A DRIVE TRAIN</b> .....	<b>5</b>
<b>4. CONDITION MONITORING SYSTEM</b> .....	<b>7</b>
<b>5. ANALYSIS AND MODELLING OF A MULTICOPTER DRIVE TRAIN</b> .....	<b>8</b>
<b>6. FAILURE IDENTIFICATION AND MODELLING</b> .....	<b>13</b>
<b>7. INFLUENCE OF FAULTS ON THE FLIGHT PERFORMANCE</b> .....	<b>14</b>
<b>8. SUMMARY</b> .....	<b>15</b>
<b>ACKNOWLEDGEMENTS</b> .....	<b>16</b>
<b>APPENDIX</b> .....	<b>16</b>
<b>REFERENCES</b> .....	<b>16</b>
<b>BIOGRAPHY</b> .....	<b>17</b>

## 1. INTRODUCTION

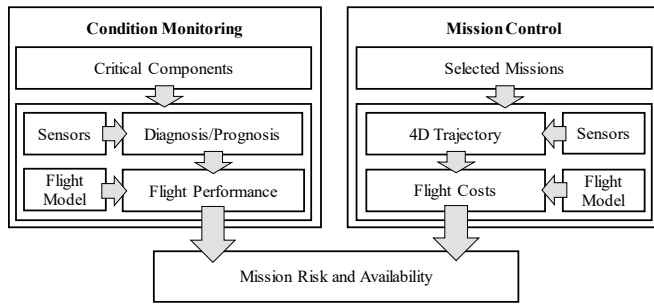
Unmanned Aircraft Systems (UAS) offer numerous applications in a wide range of fields. In addition to the military market, the commercial market is currently growing rapidly [1, 2]. For example, enormous demand is forecast for business areas such as agriculture, energy, public safety, logistics and mobility in particular. While the European drone industry currently plays only an insignificant role in these areas, the economic potential for the year 2035 is estimated to be around 10.5 billion euros and for 2050 actually 14.5 billion euros [2]. The studies assume that most of the used UAVs will be multicopters or hybrid designs, i.e. a combination of multicopter and aerial aircraft. To open up the market key technologies like the integration of UAVs into the airspace and the technical development of autonomous systems have to be investigated [3]. The degree of UAV autonomy can be categorized into different levels. A classification method according to [4] is shown in Table 1. It is assumed that the individual aircraft first will be equipped with technical systems before networking of a group of UAVs will be developed from level 5 onwards. There are currently unmanned aerial aircrafts in military service, such as the Global Hawk, which operate between autonomy levels 2 and 3. However, conventional small multicopter systems are generally located in level 1.

Table 1. Level of autonomy for UAVs [4]

1	2	3	4	5
Remotely Guided	Real Time Health Diagnostics	Adapt to Failure & Flight Conditions	Onboard Route Replan	Group Coordination
6	7	8	9	10
Group Tactical Replan	Group Tactical Goals	Distributed Control	Group Strategic Replan	Fully Autonomous Swarms

An autonomous flight reduces personnel and training costs, but places higher demands on the safety of the system. A multicopter system generates the required lift or thrust exclusively with the aid of its drive trains, which therefore essentially influence the flight performance and thus also the feasibility of a mission. A suitable system for condition monitoring of a drive train can therefore make a significant contribution to multicopter safety and enables decision making for higher levels of autonomy. Reactions to disturbances in the planned mission process could be

described using an availability value. A possible calculation procedure is shown in Figure 1. With the aid of a condition monitoring system critical components are monitored by suitable sensors. Algorithms for diagnosis and prognosis provide information about the current and prospective condition that is used in combination with a flight model to estimate the flight performance. A mission control system detects disturbances from the environment, such as unforeseen weather changes or obstacles. These have an influence on the planned trajectory. Such a mission-specific trajectory has to be time-determined using optimization criteria for efficiency or mission duration. Together with the flight model, the flight costs or the required flight performance can be determined. A comparison provides information on the availability of the UAV for the current mission, and the reserve or residual provides information on the expected mission risk.



**Figure 1. Possible procedure for calculating mission risk and availability**

In addition to the condition monitoring system with additional sensors, which is presented in this paper, there are also approaches that allow flight performance estimation with onboard sensors only [5]. These fault detection and identification (FDI) algorithms are often used to determine maximum output variables for adaptive flight controller [6]. Using model knowledge and information from the inertial measuring unit (IMU), the required thrust forces on the individual drive trains can be calculated for the current flight condition. A comparison with the commanded forces allows drawing conclusions about interference in the control loop. Such interferences can result from technical failures or environmental influences such as wind. In addition to the weight saving due to the unnecessary additional sensors, the advantages of these FDI algorithms are high performance and short calculation time. Common disadvantages are, in particular, the limited information on the exact cause of a failure. Without such information, it is not possible to forecast the future progression of a failure and thus the flight performance for the further mission progress.

Figure 2 shows an extract of a fault tree analysis (FTA) [7]. The presented error tree contains four levels. Level I describes the FTA's goal. Therefore, the focus of the considerations made here is on the cause of a decrease in thrust. The components or assemblies of the drive train are listed in Level II. A decreased thrust can result either from a reduced output power of the battery, a decreased efficiency

of the ESC, the engine or the propeller. In addition, all combinations of the effects presented above also lead to a decrease in thrust. In Level III the assemblies are further broken down into their components. Figure 2 only shows an exemplary selection, but it becomes clear that there are many reasons for a decrease in thrust. In addition, the failure progression can be very different. For example, some causes of failures lead to a sudden loss of thrust, other failures have a degrading behavior. In order to reliably estimate a decrease in thrust due to technical failures, additional sensors are required. This ensures the best possible failure identification at a high level of the FTA. For these reasons, a sensor system is introduced, that is capable of determining the current thrust force and the condition of the most important drive train components. In this way, selected failure conditions should be diagnosed and predicted.

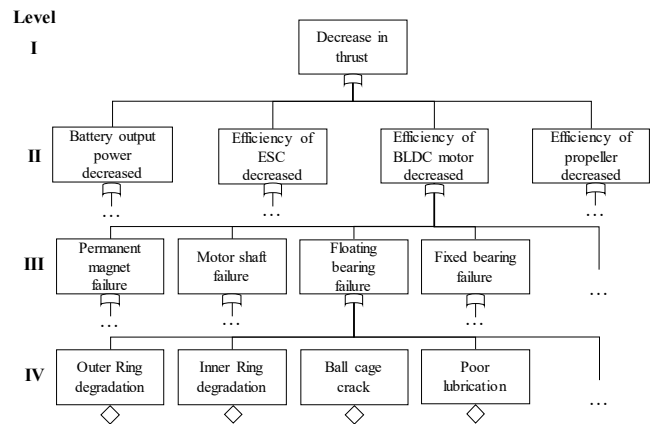


**Figure 2. Extract from the fault tree analysis of a multicopter's drive train**

## 2. FLIGHT PERFORMANCE ANALYSIS WITH A X8 TEST SYSTEM

The vehicle used for these investigations is a modified version of the X8 multicopter from 3D Robotics shown in Figure 3. Relevant copter data is summarized in Table 3 in the appendix. In addition to the well-documented APC Slow Fly 11x4.7 propellers [8], motors of the type Hacker A30-52S-UAV are installed.



**Figure 3. Picture of the unmodified X8 research copter**

The copter has four arms each with two drives in coaxial configuration. The rotors of an arm influence each other. To

be able to use the twist of flow of an upper rotor, the lower rotor turns in opposite direction. However, due to the induced axial flow velocity from the upper rotor, the thrust at the lower rotor is reduced. In section 5, it is shown that at full rotor speed the thrust of the lower rotor is only 60% of the thrust in the undisturbed case. In order to compensate torque of the individual rotors, adjacent rotors of a plane rotate in the opposite direction. All rotor rotation directions are shown in Figure 4.

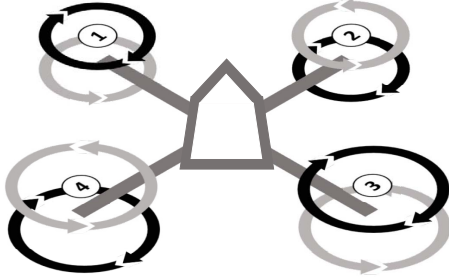


**Figure 4. Schematic overview of the X8 airframe with rotation directions of the individual drive trains**

In order to describe the flight performance of a multicopter, the knowledge gained from investigations of helicopters are very well applicable. For this reason, the following performance parameters are described using the X8 multicopter as an example.

- (1) Hover flight
- (2) Axial flight (climb and descent)
- (3) Horizontal flight
- (4) Endurance and range

#### Hover flight

Figure 5 shows the corresponding mechanical parameters for axial movement in the xz plane of the multicopter. To simplify this analysis, the thrust of the coaxial rotors at one arm is combined. In addition, the thrust of two arms is already summarized in Figure 5 as  $T_{1,2}$  or  $T_{3,4}$ .

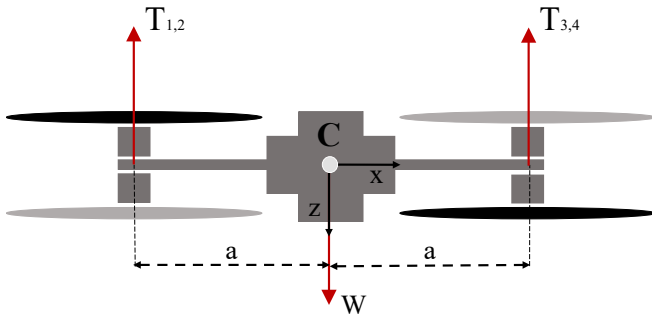


**Figure 5. Cross-section of the multicopter for schematic representation of the forces for axial movement**

The thrust forces generate a torque with the lever arm  $a$ . The weight force attacks in the center of gravity  $C$ . For axial

flight, the sum of all torques must be zero. Thus, the copter weight  $W$  and thrust  $T$  have to be in balance.

$$T_c = \sum_{k=1}^4 T_{u,k} + \delta T_{l,k} = mg \quad (1)$$

where  $T_c$  is the copters total thrust,  $u$  indexed the upper and  $l$  the lower rotors. The influence of the upper rotors on the lower rotors is described with the help of the factor  $\delta$ . According to section 5 at full thrust  $\delta$  can be approximated to 0.6. The single rotor's thrust can be estimated through the actuator disc theory, shown in Figure 6 [9–11].

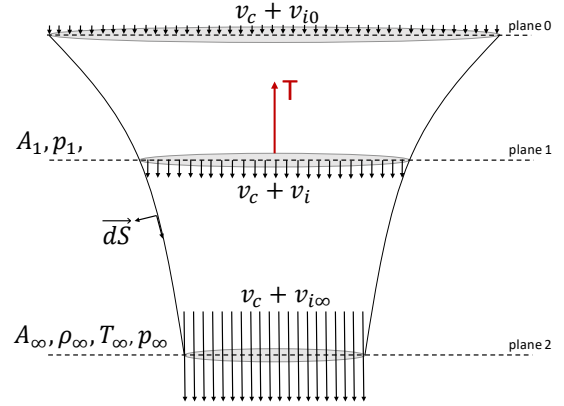


**Figure 6. Model of the flow through a propeller according to the actuator disc theory**

The air mass flow through the rotor (plane 1) is

$$\dot{m} = \rho A_1 (v_c + v_i) \quad (2)$$

where  $A_1 = \pi R^2$  is the rotor area for a radius  $R$ ,  $\rho$  is the air density,  $v_c$  is the copter velocity in z-direction and  $v_i$  is the induced velocity through the rotor. According to the momentum equation, the thrust in hovering flight is

$$T = \dot{m} \Delta V = \rho A_1 (v_c + v_i) v_{i\infty} \quad (3)$$

where  $v_{i\infty} = 2v_i$  is the velocity of the fully formed stream. For the induced power this leads to

$$P_i = \frac{1}{2} \dot{m} (2v_i)^2 = 2\rho A_1 v_i^3 = T v_i \quad (4)$$

With an estimated motor power  $P_m$  of 120 W and an efficiency of  $\eta = 0.5$  the maximum thrust of one drive is 8.15 N. The total copter thrust  $T_{c,max}$  follows with equation (1) to 52.14 N. The maximum rotor speed  $n_{max}$  can be calculated with the propeller pitch  $h$  to

$$n_{max} = \frac{v_{i\infty}}{h} \quad (5)$$

In the case of the Slow Fly 11x4,7 propellers,  $n_{\max}$  follows to 7400 rpm. The corresponding torque results with the motor power according to

$$M = \frac{P_m}{2\pi n} \quad (6)$$

Therefore,  $M_{\max}$  becomes 154.8 mNm. In Figure 7, the forces in hovering flight are plotted over the copter mass. The upper thrust limit is  $T_{\max}$ ,  $T_{0.8}$  limits the range in which there is sufficient thrust reserve for position control and maneuvers. Below this limit, the copter is considered controllable. In the case of a complete breakdown of a drive train, in hovering flight the X8 falls back to a quadcopter configuration. The relevant thrust is  $T_{\text{quad}}$  with the 80 % limit  $T_{\text{quad } 0.8}$ . The empty weight of the copter is 1.8 kg and it is shown on the left side of Figure 6 as a vertical line. For a controllable flight in quadcopter mode, a maximum payload of approximately 0.9 kg and thus a take-off mass of 2.7 kg follows. Up to a maximum mass of 3.2 kg an emergency landing after engine failure is still possible.

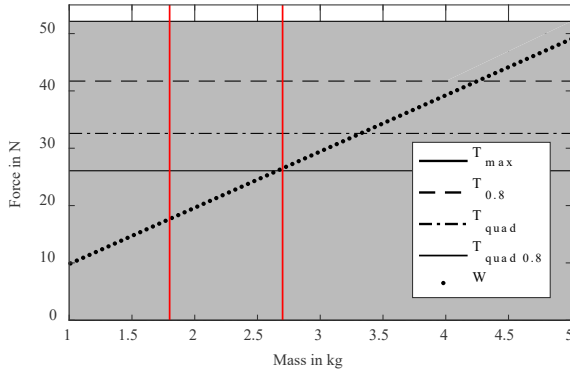


**Figure 7. Maximum Payload in hover flight for various thrust configurations**

#### Axial Flight

Climb and descent of helicopters are often described in literature [9–11]. Assuming that thrust in hovering flight ( $v_c=0$ ) is equal to the thrust in climb flight with equation (3) the ratio of induced velocities follows to

$$\left( \frac{v_c}{v_{i,h}} + \frac{v_i}{v_{i,h}} \right) \frac{v_i}{v_{i,h}} = 1 \quad (7)$$

At fast descent, flow moves in opposite direction through the rotor. The correlation of induced velocities is shown in Figure 8. Hovering is defined for  $v_z/v_{ih} = 0$ . For  $v_z/v_{ih} < 0$  the copter descends. Between the curves for slow and fast descent, the line for autorotation ( $v_c = -v_i$ ) is drawn. The transition between the two states is shown by an exponential fit [10]. In order to ensure yaw stability, a slow descent is usually performed by multicopters. However, the vortex ring state also occurs in this area. Generally, the smaller the multirotor the more likely it is to suffer from this effect. Therefore  $v_z/v_{ih} \geq -1$  is recommended for rate of descend. From these constraints, the

induced velocity in hovering flight and the maximum descend speed is  $v_{ih} = -v_{z\max} = 5.24$  m/s for the X8.

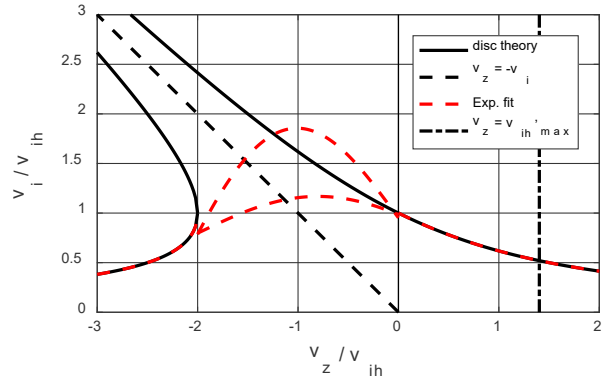


**Figure 8. Influence of axial airspeed on induced velocity based on [9]**

For  $v_z/v_{ih} > 0$  the copter climbs. If  $v_z = v_{ih\max} = 7.36$  m/s, the thrust becomes zero according to equation 3. However, when climbing the air resistance must also be taken into account. As a consequence the maximum climb speed  $v_{z,m}$  results from Newton's first law as

$$v_{z,m} = -2k \frac{A_1}{A_{cz}c_{dz}} v_i \pm \sqrt{\left( 2k \frac{A_1}{A_{cz}c_{dz}} v_i \right)^2 - \frac{2mg}{\rho A_{cz}} + 2k \frac{A_1}{A_{cz}c_{dz}} v_i^2} \quad (8)$$

where  $A_{cz}$  is the copters flow-effective area in the xy plane,  $c_d$  is the drag coefficient in z-direction and  $k$  the thrust factor according to equation (1). With  $v_i = v_{i\max}$  the maximum climb speed for the X8 follows to 2.96 m/s.

#### Horizontal Flight

Figure 9 shows the relevant forces for horizontal movement in x-direction. To generate a force in this direction, the copter is tilted by pitch angle  $-\theta$ . Thus, the thrust vector is split in a vertical part  $L = \cos(-\theta)T$  and a horizontal part  $T_x = \sin(-\theta)T$ . With the weight  $W$  and the air drag  $D$  follows the equilibrium of forces:

$$\begin{aligned} \uparrow : \quad W &= mg = L = \cos(-\theta) T \\ \leftarrow : \quad D &= \frac{1}{2} \rho v_x^2 A_{cx} c_{dx} = T_x = \sin(-\theta) T \end{aligned} \quad (9)$$

Similar to the axial flight, the assumption of constant inflow conditions via the actuator disc theory is made again [10]. Thus, the total velocity  $v_t$  through the rotor follows from the flight velocity  $v_{cx}$  and the induced velocity  $v_i$  to

$$v_t = \sqrt{v_{cx}^2 - 2v_i v_{cx} \sin \alpha + v_i^2} \quad (10)$$

where  $\alpha$  is the angle of attack between flow and rotor plane. For high velocities  $v_{cx}$  or low rotor speeds  $\alpha = \theta$  can be assumed.

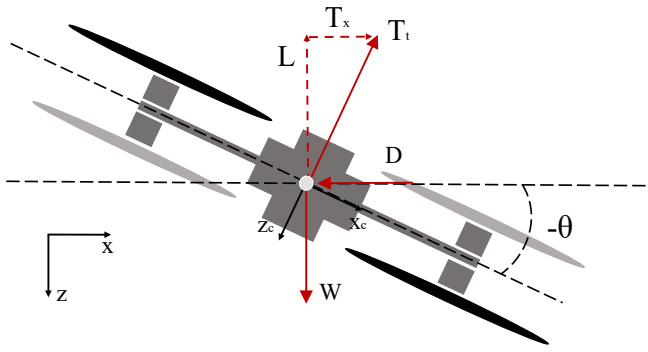


**Figure 9. Cross-section of the multicopter for schematic representation of the forces for horizontal flight**

The forces in earth coordinates according to equation (9) are shown in Figure 10. Again a maximum flow velocity of  $v_t = v_{i\_max}$  and a constant effective air drag surface  $A_{cx}$  are assumed. With these assumptions, the maximum velocity in x-direction follows to  $v_{xmax} = 17$  m/s at a pitch of 12 deg.

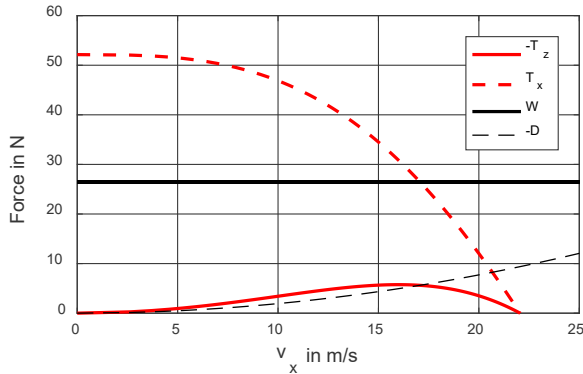


**Figure 10. Forces in earth coordinates for horizontal flight without loss of thrust**

#### Endurance / Range

For helicopters, the required power for horizontal flight is divided into induced power, parasite power and profile power. From equation (10) it can be seen that the power required to generate the induced velocity in the rotor decreases at high speeds, since the components of  $v_x$  influence the air mass flow through the rotor. However, this effect only occurs at high velocities of more than 14 m/s. Since the horizontal cruising speed of the X8 is low, this effect is neglected and only a simple performance evaluation is carried out [12]. From equation (4) follows the required power in hovering flight  $P_{ih} = 42.7$  W. The required total power is calculated together with the total efficiency  $\eta = 0.5$  to 85.7 W. This results in a maximal flight time of 10 minutes with the eight drive trains and a LiPo battery with a capacity of 8000 mAh. In horizontal flight at maximum speed, the required power per drive train is 120 W. This leads to a flight time of 7 min and a range of 7500 m.

### 3. COMPONENTS OF A DRIVE TRAIN

Most multicopters below a gross weight of 20 kg have an electromechanical drive train as shown in Figure 11.

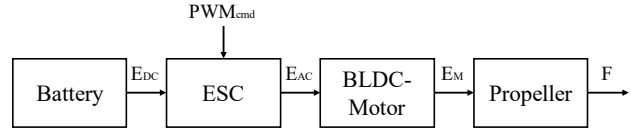


**Figure 11. Schematic of a multicopter drive train**

The energy source is a battery, which supplies the electronic speed controller (ESC) with direct current. The ESC transforms this energy into alternating current for the brushless direct current motor (BLDC-Motor) which produces mechanical power. The flight controller uses a pulse width modulated (PWM) signal to adjust the power output. The mechanical power after the BLDC motor drives a rigid propeller with a constant pitch to accelerate air and thus to produce the desired thrust.

#### Battery

The energy storage for multicopter systems is usually a lithium polymer battery. The nominal voltage per cell is 3.7 V. Depending on the needed thrust and size of the multicopter the battery contains a different number of cells. In the common weight class of 1 to 5 kg batteries with 4 or 5 cells are used. This results in a nominal battery voltage of 14.8 to 18.5 V. The actual battery voltage has a significant impact on the thrust production of the drive drain. During flight the battery will discharge, which leads to a voltage drop. Depending on the state of charge the voltage per cell is between 3.5 and 4.3 V. Figure 12 shows the impact of the current state of charge on the produced thrust [13, 14]. The thrust decreases significantly during flight due to battery discharge. This has a notable impact on the mission based availability of the multicopter system.

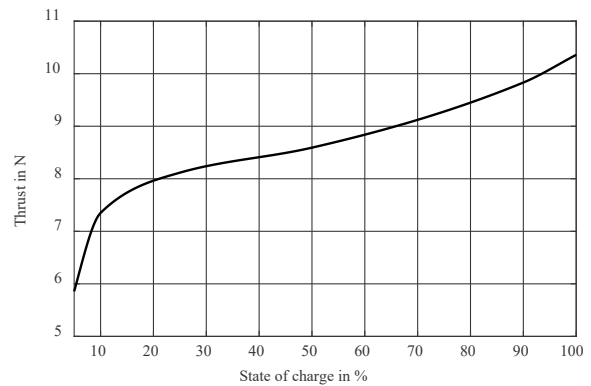


**Figure 12. Power train thrust production over state of charge of the lithium battery [14]**

#### Motor and ESC

The functional principle of a BLDC motor is the same as for a permanent magnet synchronous motor (PMSM). The sole difference is the shape of the alternating supply current. Instead of a sinusoidal shape for a PMSM, the BLDC motor

is driven by a trapezoidal, block commutated direct current [15]. Multicopter motors usually have an external rotor. This means that the rotor with its permanent magnets is external and the stator with its windings is internal. The coils of the stator are wired together to three phases. Figure 13 shows the electric control of the different phases, which are linked together in a star connection. At any time, current runs through two of the three phases. Each phase is controlled by the ESC, which is on the left side in Figure 13.

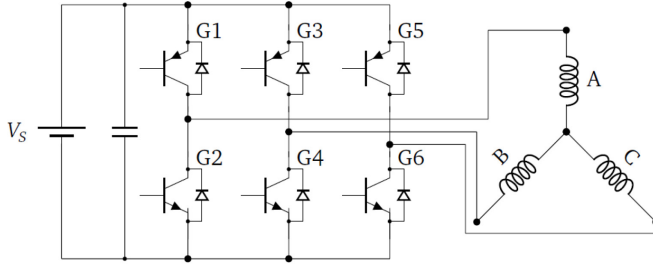


**Figure 13. Schematic of the ESC and motor circuit**

The ESC is connected to the battery. In order to drive the motor, the ESC energizes each phase in six sequences per electric cycle. The flow of the current is controlled by transistors. In Figure 13 these components are named G1 to G6. Due to the coil inductances, current spikes occur at each sequence, therefore, free-wheeling diodes are needed to dissipate the energy stored in the coils.

To ensure minimal torque ripples, electric sequences have to match the current rotor position. The synchronization of mechanical and electrical system can be done sensorless or with Hall sensors [16]. Due to the small size of the motor and production costs, multicopter BLDC motors usually do not have integrated Hall sensors. The sensorless drive is based on the detection of the back electromagnetic force (BEMF) induced by the movement of the permanent magnet rotor in front of the stator winding. For this method the zero crossings of the induced voltage in the non-energized phase are measured and converted into drive signals for the transistor commutation. [17]

The ESC cannot only drive the motor but also control the motor speed. The flight controller transmits the desired speed via a PWM signal. The frequency bandwidth of commonly used ESCs reaches from 50 to 495 Hz. The ESC converts this signal into a needed supply voltage of the BLDC motor. The effective supply voltage is then adjusted by a PWM control with a frequency of 8 or 16 kHz.

The electric power consumption of the ESC and motor can be calculated with following equation:

$$P_{el,DC} = V_s(t)I_s(t) \quad (11)$$

where  $V_s(t)$  is the supply voltage and  $I_s(t)$  is the direct current consumed.

The mechanical output power is determined by

$$P_M = 2\pi nM \quad (12)$$

where  $n$  is the rotational speed of the rotor and  $M$  the mechanical torque produced.

The combination of equation (11) and (12) leads to the calculation of the combined efficiency of the ESC and motor:

$$\eta_{ME} = \frac{P_M}{P_{el,DC}} \quad (13)$$

### Propeller

Propeller used in multicopter systems have a fixed pitch. Therefore, a variation of thrust can only be done by a variation of the rotational speed of the motor. The thrust develops through jet reaction. The propeller accelerates a fluid mass, in this case ambient air [18]. Due to Newton's law a reactive force is then applied on the multicopter.

As shown in Figure 6, the inflow velocity  $v_c$  is increased by  $\Delta v$  due to the pressure difference directly in front of and after the propeller. In the case of static thrust ( $v_c = 0$ ), the produced thrust  $T_0$  can be calculated by

$$T_0 = A_1 \rho \frac{\Delta v}{2} \quad (14)$$

where  $A_1$  is the propeller area,  $\rho$  the air density and  $\Delta v$  the jet velocity.  $\Delta v$  can be determined by measuring the dynamic pressure with a Prandtl tube. According to Bernoulli's equation the jet velocity is expressed as:

$$\Delta v = \sqrt{\frac{2 p_{dyn}}{\rho}} \quad (15)$$

where  $p_{dyn}$  is the dynamic pressure.

Therefore, the static thrust  $T_0$  can be calculated as:

$$T_0 = A_1 p_{dyn} \quad (16)$$

The static thrust power is developed with the kinetic power of the produced jet stream:

$$P_L = \frac{1}{2} A_\infty \rho \Delta w^3 \quad (17)$$

where  $A_\infty$  is the contracted area of the stream after the propeller.

For the later simulation of the propeller the coefficient for thrust and power are also important. These values depend on the Reynolds number and the blade geometry of the propeller. The dimensionless thrust coefficient  $C_T$  is defined as:

$$C_T = \frac{T}{\rho n^2 D^4} \quad (18)$$

where  $T$  is the thrust,  $n$  the rotational speed and  $D$  the diameter of the propeller.

Similarly, the power coefficient  $C_P$  is expressed as:



$$C_P = \frac{P}{\rho n^3 D^5} \quad (19)$$

where P is the mechanical shaft power needed to drive the propeller.

#### 4. CONDITION MONITORING SYSTEM

Requirements for the CM system were derived by failure tree analyses and a Failure Mode and Effect Analyses (FMECA) [7]. Figure 14 shows an overview of the measurement concept. Current and voltage sensors located between the battery and the ESC are used to determine the ESC input power and provide information about the battery status. Other current and voltage sensors in the phase supply cables between ESC and motor provide information about the input power in the BLDC motor. In addition, the motor speed and torque can be estimated by means of the currents. The voltages contain information about possible short circuits. Thermocouples on BLDC motors and ESCs, as well as a vibration sensor, are intended to help to identify the causes of faults more closely and enable decision making in the event of unclear conditions. Prandtl probes can be used to determine the output power of a drive train by measuring the dynamic pressure. One Prandtl probe determines the undisturbed flow component, a further probe is mounted under the propeller, whereby a determination of  $v_i$  and thus of the thrust is possible. Other sensors measure the ambient data such as humidity, air pressure or temperature.

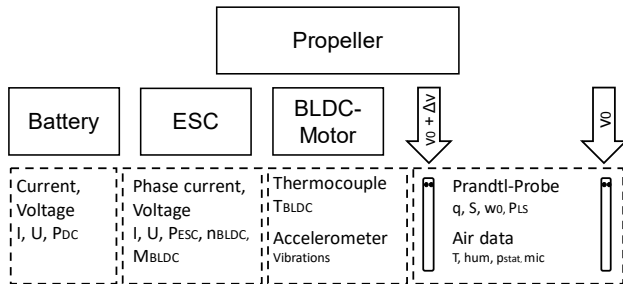


**Figure 14. Sensor suite concept for condition monitoring of a drive train in multirotor UAVs**

The determination of the drive train condition has to be carried out with the aid of the measured data based on a performance analysis. This enables not only to determine the current thrust power, but can be also used together with other sensors to identify the main component in which the fault occurred.

##### Test rig

In order to examine the CM system presented above and to analyze failures of the drive train, a test rig is required. Figure 15 shows an overview of the employed test rig. The unit under test (motor with propeller) is mounted centrally on a sensor line (no.3). The measurement section (no.2) is enclosed laterally with transparent PET and it allows the investigation of propellers with a maximum diameter of 12 inches. The ESC is located outside the measuring section in one of the electronics housings (no.6). The electronics

housings also contain sensors for determination of the three phase currents and voltages as well as the ESC input current and the ESC input voltage. An analog-to-digital converter (A/D converter) processes the measured data and makes them available to the computer (no.4). High-precision laboratory power supplies (no.5) provide the power of the sensors and the unit under test. The operator controls and monitors the experiment using a touch screen (no.1).

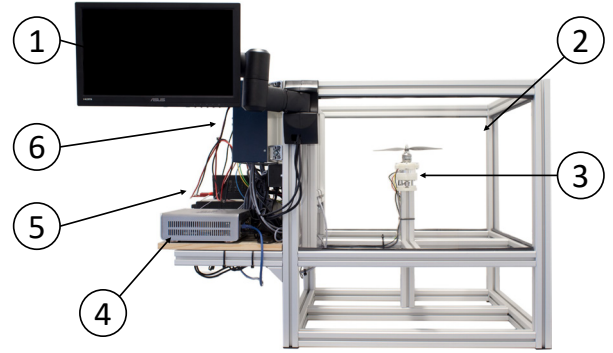


**Figure 15. Overview test rig – touch screen (1), measurement section (2), sensor line (3), computer (4), power supplies (5), el. power sensors (6)**

##### Sensors

In addition to the already mentioned sensors for current and voltage measurement, further sensors are integrated in the test rig. Not to be seen in Figure 15 is the Prandtl probe for the determination of dynamic pressure, which is mounted underneath the unit under test. The probe absorbs the pressure at a distance of approximately 80 mm from the pivot point and 40 mm below the propeller mount. The pressure is transmitted via 0.5 m long pressure tubes to a high-precision differential pressure gauge. Further sensors are located in the sensor line illustrated in Figure 16. The unit under test (no.1) is attached to an adapter plate (no.2). This includes a thermocouple of type K to measure the motor temperature. A torque sensor (no.3) connects the upper plates with the lower structure. The sensor measures the reactive torque with the aid of strain gauges.

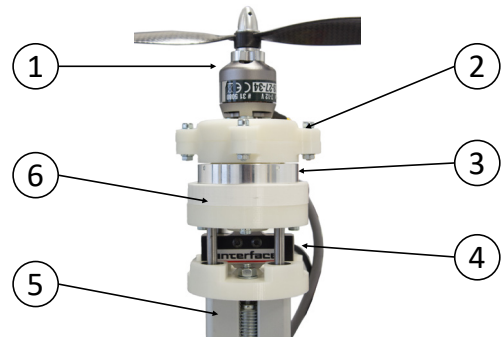


**Figure 16. Overview line sensors rig – BLDC motor with propeller (1), thermocouple (2), torque sensor (3), force sensor (4), microphone (5), vibration sensor (6)**

A vibration sensor is integrated in the lower body (no.6). Below is a force sensor (no.4), which measures the axial thrust. To protect the sensor against lateral forces, slide-bearing guides have been installed. In addition, a small microphone is attached to the body (no.5). Furthermore, the temperatures of the ESC and the ambient environment are measured. The A/D converter, which records and processes the data at a frequency of 50 kHz, is the main component of the measuring system. Further analog sensors can be integrated quickly and easily for testing purposes. In addition, it is possible to connect and test digital sensors via specially developed interfaces to Arduino microcontrollers.

#### *Evaluation of the sensor concept*

Most of the presented sensors are well suited for use within the test environment, but not for use in a multicopter. In addition, the use of expensive sensors in a small multicopter is not feasible. Therefore, the individual sensors should be evaluated. Since numerous failures result in strong vibrations, acceleration sensors are very well suited for fault detection. During flight, however, the accelerations of the multicopter movement are overlaid here. The question of the possibilities of predicting failure cases still needs to be investigated. Components of the drive train should not be modified to integrate additional sensors. Therefore, torque sensors mounted on the shaft cannot be used. However, the measurement of the reactive torque is only suitable as a reference for static use in the test rig, since dynamic effects cannot be measured correctly. Similar to acceleration sensors, additional forces are overlaid during force measurement in flight. In addition, the price of strain gauge-based sensors often exceeds the price of a complete copter system. The measurement of electrical currents and voltages has turned out to be very successful. They enable a performance evaluation of the electrical components and can be used to measure the engine speed as well. It has been proven that microphones are suitable for recording the airscrew speed. In addition, the acoustic signals resulting from various failures can be recorded. During flight operations, however, the signals of all drive trains and those of the environment overlap each other. Nevertheless, the application should be investigated in more detail, as the sensors are very inexpensive and easy to use. Components in a failure condition often lose efficiency. The performance is often lost in form of heat, which is the main reasons for establishing temperature sensors as the standard in the field of condition monitoring.

As shown in equation (16), the static thrust can be determined by a dynamic pressure measurement. Figure 17 shows the comparison of the determined thrusts from the force sensor and the calculation from the dynamic pressure. It should be noted that the velocity  $\Delta v$  is determined by the dynamic pressure is only measured at one position. In addition, an adjustment to the reduced surface area  $A$  has not been taken into account. However, the determined curve can be exactly transferred to the force curve by multiplying it with a compensation factor. If the latency time in the signal resulting

from the pressure tubes is taken into account, the dynamic pressure measurement is suitable for determining the thrust. For the use in a multicopter, however, the air velocity  $v_c$  has to be determined, for which a further Prandtl probe can be used.

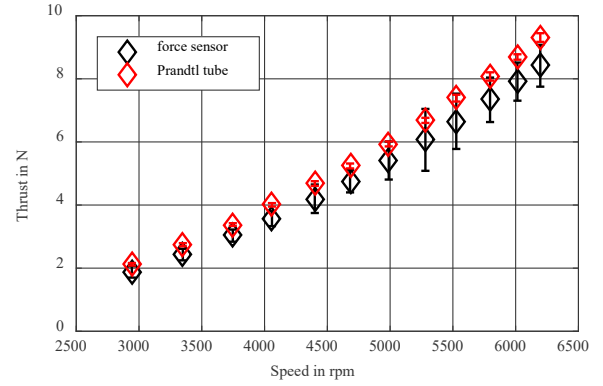


**Figure 17. Comparison between force sensor and Prandtl tube measurement**

Figure 18 shows the frequency spectrum of phase current, vibration sensor and microphone signals. Amplitude peaks at frequencies greater than 1 Hz can be used to determine the speed of motor or propeller. While current sensors determine the engine speed, the other sensors provide information about the propeller speed.

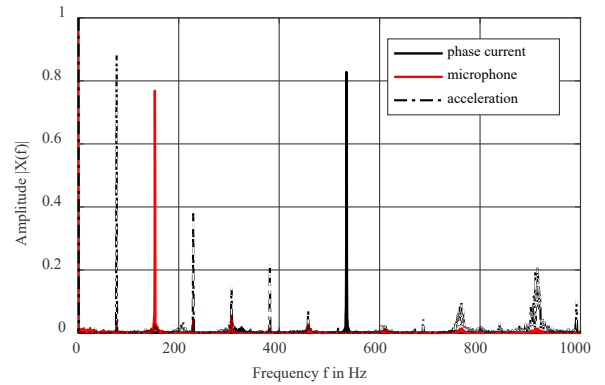


**Figure 18. Signals from microphone, current and vibration sensor in the frequency range**

## **5. ANALYSIS AND MODELLING OF A MULTICOPTER DRIVE TRAIN**

Following section describes the numerical simulation of the components of a multicopter drive to develop algorithms for the calculation of availability of multicopter system in the future. Main input variable of this system is the supply voltage  $V_S$ . The ESC system transforms this voltage in an alternating voltage for the motor-subsystem. This subsystem simulates the electrical and mechanical behavior of the BLDC motor based on mathematical equations. Furthermore, a system for the simulation of the propeller is included which calculates thrust and load torque of the motor. This model is



able simulate correctly the behavior of a multicopter's faultless drive train as well as the impact of faults on characteristic parameters of the motor and propeller. Induced vibrations and their impact on components are not in the focus of this model.

#### Mathematical model of the ESC and BLDC

The equations for the electrical (20) and the mechanical (21) system are transformed into a state space model. This allows a very efficient numerical simulation with Simulink. The basic equation of the electrical system is:

$$u_{ab} = R(i_a - i_b) + L(\dot{i}_a - \dot{i}_b) + e_a - e_b \quad (20)$$

where  $R$  is the phase resistance,  $L$  the phase inductance,  $i_i$  the phase current,  $e_i$  the back electromagnetic force (EMF) of each phase and  $u_{ab}$  the line voltage.

The mechanical system is represented by:

$$T_e - T_l = \ddot{\theta}_m J + \dot{\theta}_m k_f \quad (21)$$

where  $T_e$  is the torque produced by the motor,  $T_l$  the load torque of the propeller,  $\theta_m$  the mechanical angle of the rotor,  $J$  the moment of inertia and  $k_f$  the dynamic friction coefficient.

For a BLDC motor the conducting region of phase current corresponds to the peak value segment of the back EMF, hence, the electromagnetic torque can be calculated by:

$$T_e = \frac{e_a i_a + e_b i_b + e_c i_c}{\dot{\theta}_m} \quad (22)$$

The implementation of the described equations in Simulink is schematically shown in Figure 19. This schematic also shows the calculation of the trapezoidal back EMF. Besides the load torque of the propeller, there is also a static friction torque affecting the BLDC motor.

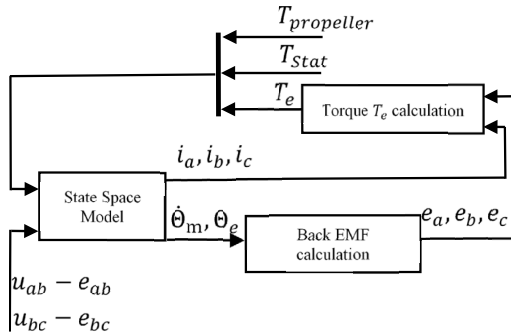


**Figure 19. Schematic of the mathematical model of the multicopter drive train in Simulink**

This model is able to simulate the drive drain very realistically which can be seen in comparison with the test data. Figure 20 shows the motor phase current of the real drive train and its model. A very close match of model and test data can be observed.

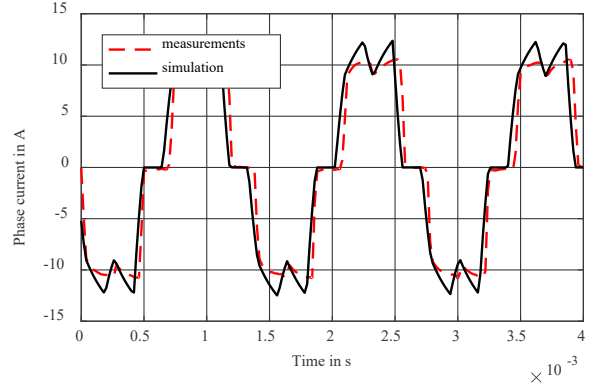


**Figure 20. Comparison of the phase current of the model and a real drive train**

#### Propeller

The propeller is modelled with the thrust and power coefficients. These coefficients were determined with multiple test runs of a Slow Fly 11x4.7 propeller and a linear regression analysis. Figure 21 shows the results of this analysis for the power coefficient  $C_p$  of the propeller.

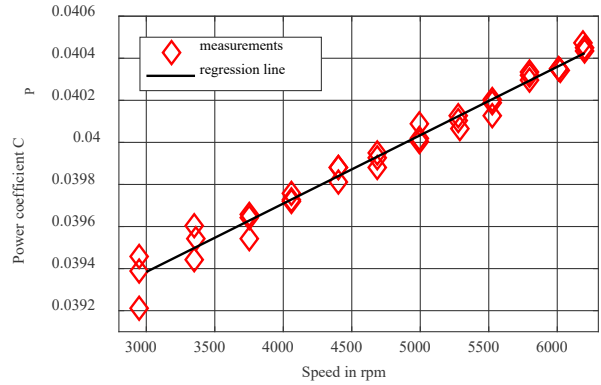


**Figure 21. Regression analysis of the power coefficient**

The proposed model calculates thrust and load torque based on the current speed of the motor and the coefficients of the propeller. This kind of partly databased modelling results in very realistic simulation of the actual drive train.

#### Coaxial propulsion system

The coaxial propellers are mounted at a distance of 0.13 meters. The model for the coaxial rotor is developed using the commonly accepted blade element momentum theory (BEMT), which is a hybrid method for rotor analysis. It combines the principles of Rankine's momentum theory with the blade element theory developed by Froude. The BEMT is based on the equivalence between the circulation and momentum theories of lift while applying the conservation laws to an annulus of the rotor disk and is described in many different articles [19, 20]. Figure 22 and Figure 23 show the BEMT flow model for the coaxial propulsion system.

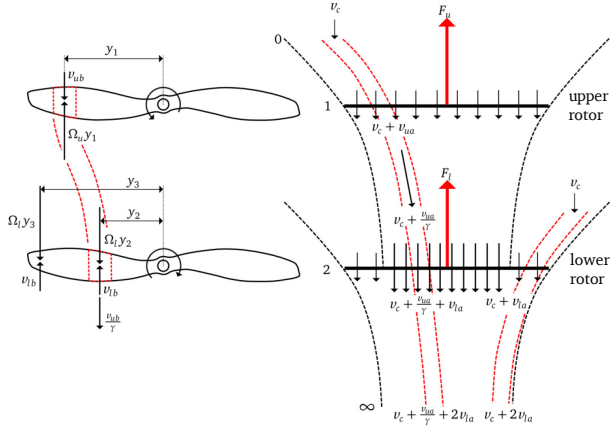


**Figure 22. BEMT flow model in rotational (left-side) and axial (right-side) direction for coaxial rotors**

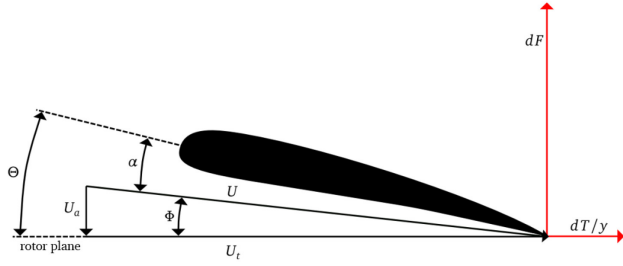


**Figure 23. Propeller - Blade element section**

The model assumes that the lower rotor operates partly in the slipstream of the upper rotor. The outer part of the lower rotor is assumed to be not affected by the upper rotor. It is also assumed that the lower rotor does not affect the upper rotor. Momentum theory states that the slipstreams surface of the upper rotor  $A_\gamma$ , hitting the inner part of the lower rotor, decreases with the distance between the rotor planes. Because of conservation of mass, the slipstream velocity of the upper rotor increases the more it is contracted. The contraction of the wake is taken into account by the factor  $\gamma$ , where  $A_1$  is the upper rotors total surface.

$$\gamma = \frac{A_\gamma}{A_1} \quad (23)$$

Using blade element theory, the thrust  $dF$  and torque  $dT$  generated by a blade element is calculated by:

$$dF = \frac{1}{2} \rho U^2 c N_b (C_l \cos \phi - C_d \sin \phi) dy \quad (24)$$

$$dT = \frac{1}{2} \rho U^2 c N_b y (C_l \sin \phi + C_d \cos \phi) dy \quad (25)$$

where  $U$  is the relative flow velocity,  $\phi$  the angle from the rotor plane to the relative velocity vector,  $c$  the chord length of the blade element,  $y$  the distance of the blade element from the hub,  $dy$  the width of the blade element,  $N_b$  the number of blades,  $C_l$  the lift coefficient and  $C_d$  the drag coefficient.

Using momentum theory, the thrust and torque for the annulus swept by the blade element of the upper rotor is calculated by:

$$dF = \rho 4 \pi y v_c^2 (1 + a) a dy \quad (26)$$

$$dT = \rho 4 \pi y^3 v_c (1 + a) b \Omega dy \quad (27)$$

where  $v_c$  is the vertical velocity of the multicopter,  $a$  the axial inflow factor,  $b$  the angular inflow factor (swirl factor) and  $\Omega$  the angular velocity of the rotor.

Because the inflow factors  $a$  and  $b$  are initially unknown, the thrust and torque of each blade element must be calculated using an iterative approach. It starts with some initial guess of the inflow factors  $a$  and  $b$ . Taking the example of the upper rotor the flow angles  $\phi$  and  $\alpha$  can be determined using the following equations:

$$U_a = v_c + v_{ua} = v_c (1 + a) \quad (28)$$

$$U_t = \Omega y - v_{ub} = \Omega y (1 - b) \quad (29)$$

$$U = \sqrt{U_a^2 + U_t^2} \quad (30)$$

$$\phi = \tan^{-1} \frac{U_a}{U_t} \quad (31)$$

$$\alpha = \Theta_r - \phi \quad (32)$$

where  $U_a$  is the local flow velocity in axial direction,  $v_{ua}$  the induced velocity by the upper rotor in axial direction,  $U_t$  the local flow velocity in rotational direction,  $v_{ub}$  the induced velocity by the upper rotor in rotational direction,  $\alpha$  the local angle of attack and  $\Theta_r$  the angle from the rotor plane to the blade chord.

With the flow angles  $\phi$  and  $\alpha$ , the blade section properties of the blade element can now be estimated, using aero foil data from measurements or approximation functions. After that, it is possible to calculate approximate values of the thrust and torque using the equations (24) and (25). These results can then be used in equation (26) and (27) to improve the estimates of the inflow factors  $a$  and  $b$ . This process is repeated until the inflow factors have converged to within a specified tolerance. To calculate the total thrust and torque of the rotor, it is only necessary to sum up the thrust and torque for each blade element. The procedure to calculate thrust and torque for the lower rotor is the same, except the additional flow induced by the upper rotor has to be taken into account.

#### Validation of the coaxial propulsion model

For the validation of the rotor model, the influence of the two rotors is investigated with the test rig described in section 4. In Figure 24 the coaxial propulsion system of the used multicopter is illustrated. Figure 25 shows the measurement data of the thrust produced by the upper rotor for different rotor speeds of the lower rotor. As one can see, the characteristic curves for different PWM signals of the lower rotor, which are related to the speed of the lower rotor, are very close together. This means that there is an influence of

the lower rotor on the upper one, but it is very low. Subsequently, the neglect of the lower rotor's influence on the upper rotor is justified.

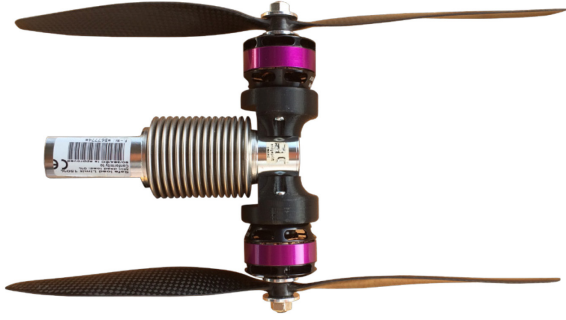


**Figure 24. Coaxial rotor attached to a bending beam load cell**

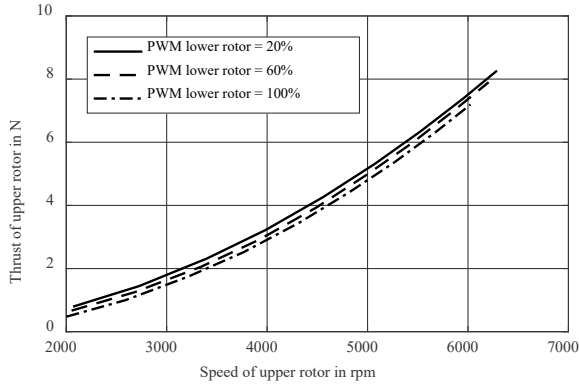


**Figure 25. Characteristic diagram for thrust of the upper rotor – influenced by lower rotor**

Because there is no information available on which aero foil design is used for the APC Slow Flyer 11x4.7, the following approximation functions are used to calculate the lift and drag coefficients  $C_l$  and  $C_d$  for the rotor model [21].

$$C_{l\alpha} = \frac{0.24}{\sqrt{1 - M^2}} \quad (33)$$

$$C_l = C_{l\alpha} \alpha \quad (34)$$

$$C_d = 0.035 + (-0.25\alpha + 0.12\alpha^2) \cdot 10^{-3} \quad (35)$$

where  $M$  is the Mach number of the corresponding blade element. By modifying the approximation coefficients, it is possible to fit the rotor model to the experimental data for the used rotor profile. The fitting of the approximation functions is performed with measurement data of an undisturbed, single rotor. Figure 26 and Figure 27 show the thrust and torque produced by an undisturbed, single rotor including the fitted data of the simulation model in hovering flight. As one can see, the developed BEMT model performs very well in simulating the behavior of an undisturbed, single rotor. Since the coaxial rotor model neglects any disturbances on the

upper rotor, the upper rotor uses the model of the undisturbed single rotor.

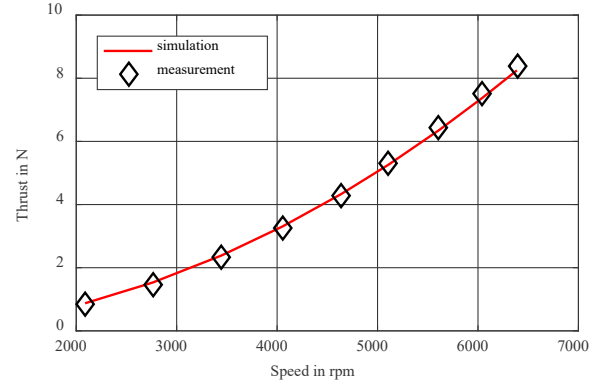


**Figure 26. Thrust of undisturbed, single rotor in hovering flight**

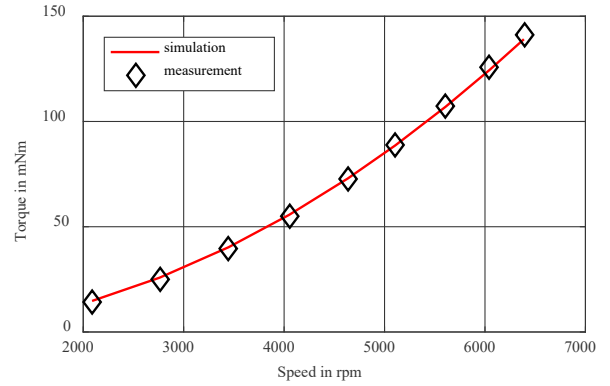


**Figure 27. Torque of undisturbed, single rotor in hovering flight**

Figure 28 and Figure 29 show the thrust and torque produced by the lower rotor for different rotor speeds of the upper rotor in hovering flight.

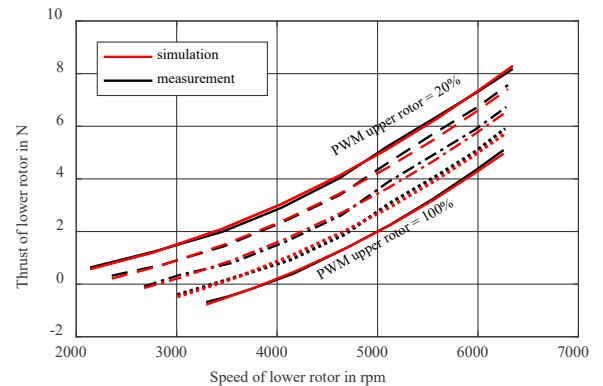


**Figure 28. Characteristic diagram for thrust of the lower rotor in hovering flight– influenced by the upper rotor**

The different curves represent constant PWM signals (20%, 40%, 60%, 80%, 100%) for the upper rotor. In contrast to the previously discussed upper rotor, one can see that the lower

rotor is largely influenced by the upper rotor. The more the rotational speed of the upper rotor increases, the more the produced thrust and torque of the lower rotor decreases. At a rotor speed of 6000 rpm of the upper rotor, for example, the maximum thrust reduction, due to the upper rotor in comparison to the undisturbed case, is 40.6 %. That results from the fact that the lower rotor operates partly in the slipstream of the upper rotor. The slipstream of the upper rotor causes the inner part of the lower rotor to operate in a climbing condition, changing the relative flow velocity and angle, which in return leads to less thrust and torque produced by the lower rotor. In contrast to the upper rotor the simulation of the lower rotor considers the disturbance of the upper rotor. Figure 28 also shows that the thrust characteristics of the lower rotor are well represented by the simulation. Figure 29 shows a good qualitative agreement with the measurement in relation to the slope and course of the diagram. However, the influence of the upper rotor is slightly overestimated in the current state of the rotor model. This overestimation is still being investigated.

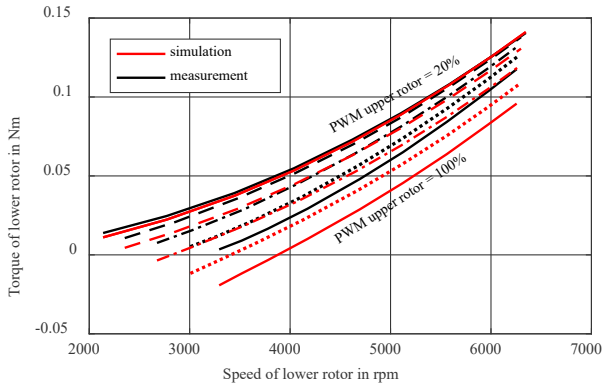


**Figure 29. Characteristic diagram for torque of the lower rotor in hovering flight – influenced by the upper rotor**

Another interesting result can be seen in Figure 30, which shows the influence of the upper rotor on the rotational speed of the lower rotor. The different curves represent constant PWM signals (20%, 40%, 60%, 80%, 100%) for the lower rotor.

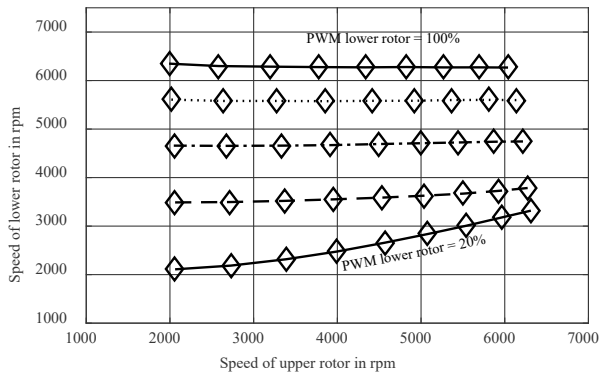


**Figure 30. Influence on rotational speed of the lower rotor depending on the speed of the upper rotor**

The rotating magnetic field created by the BLDC is directly linked to the PWM signal of the ESC. However, Figure 30 shows that the upper rotor has a large influence on the rotational speed of the lower rotor if it is rotating at a low rotational speed. If the lower rotor spins at high rotational speeds, it seems to be more robust against disturbances of the upper rotor.

### Simulation environment

In order to analyze the impact of component failure on the flight performance of the multicopter a simulation environment has been developed. Figure 31 shows the main components of the simulation environment.

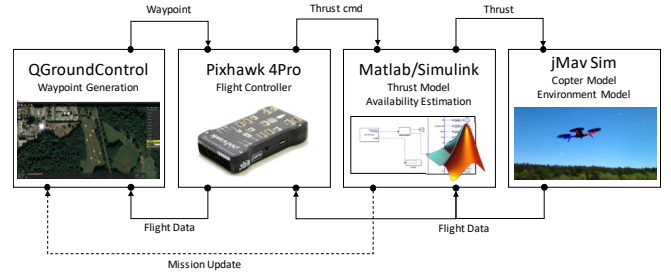


**Figure 31. Main components of the simulation environment for mission risk analysis**

**QGroundControl:** The flight control and mission planning of a multicopter is usually achieved with a ground control station. On the one hand, it enables the pilot to send specific commands, e.g. “take off” or “land”, to the multicopter as well as planning autonomous missions. On the other hand, the ground control station receives the current flight data of the multicopter, e.g. attitude, altitude, position, velocity. The ground control station, used to interact with the simulation, is the open source tool “QGroundControl” which can handle ArduPilot or PX4 Pro powered vehicles.

**Pixhawk:** The flight control unit (FCU), which is used for the X8 multicopter, is the “Pixhawk 4Pro” developed by the PX4 open hardware project. In order to achieve the same flight characteristics as the X8, with regards to the control algorithm, the simulation uses the same PX4 controller firmware for the control of the multicopter and the communication with the ground control station. For this purpose, the PX4 firmware already offers a special simulation mode.

**jMAVSIM:** The open source multicopter simulator jMAVSIM offers a complete multicopter simulation by connecting to the hardware-in-the-loop or software-in-the-loop instance of the PX4 autopilot. In the developed simulation environment, the internal rotor model of jMAVSIM is overridden by the thrust and torque data calculated in the external Matlab Simulink model. The communication between jMAVSIM and Matlab Simulink is achieved by an UDP network interface. For a given time step in jMAVSIM the current control instructions are sent to the external rotor model. After calculating the corresponding

thrust and torque values they are sent back to the jMAVSIM simulation.

**Matlab:** To achieve the same flight characteristics as in reality, a model of the propulsion system is implemented in Matlab Simulink. On the one hand, it is possible to create a propulsion model, which is based on a lookup table created by the measurement data. On the other hand, it is possible to implement the described BEMT propulsion model directly. The BEMT model allows to simulate the influence of fault behavior of the propulsion system. This makes it possible to analyze the influence of component failure on the flight performance estimation.

## 6. FAILURE IDENTIFICATION AND MODELLING

Faults that are expected to be identified by a CM system were analyzed with the help of an FMECA and listed in Table 2 [7]. Mechanical damage of the propeller (no.1) occurs very easily during operation of the drive train. For example, collisions with obstacles can quickly lead to notches in the propeller. Smaller foreign objects such as sand or dust damage the surface of the propeller (no.2). It is assumed that the rough surface leads to an increase in air resistance and therefore a higher torque of the engine is required. Bearing failures are the most common cause of breakdown of electrical motors with a rate of 40 to 50 % and have already been investigated in numerous studies [22, 23]. To consider this fault, an increased torque is assumed, which results from the increased friction. Short-circuits in the windings of the coil (no.4) can be caused in particular by foreign bodies. Especially the flight through rain is a major risk.

**Table 2. Investigated fault states**

No.	Component	Fault	RPN
1	Propeller	Mechanical damage – notch fault	210
2	Propeller	Abrasion of the propeller surface	160
3	Motor	Bearing damage - Fixed bearing	252
4	Motor	Winding short-circuit	168

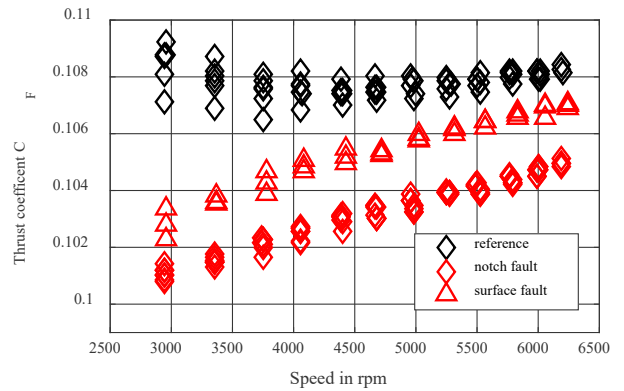
The experiments were divided into sections in which the speed was stepwise raised and lowered. The range between 0 and 100 % thrust was divided into 13 steps. On each stage, the speed was kept constant for 15 seconds. A complete interval has a duration of approx. 6 minutes and was run four times.

### Propeller faults

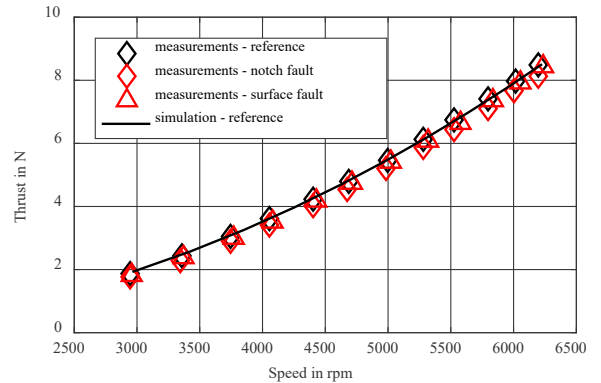
This paper investigates two main propeller faults, namely, a mechanical damage in form of a notch and the abrasion of the propeller surface. These faults were artificially applied on the propeller. The notch fault was applied as a triangular shaped notch with a depth and width of 4 mm on one side of the propeller. The surface damage was applied with a medium coarse sandpaper on the whole surface of the propeller.

Figure 32 shows the impact of the faults on the thrust coefficient of the propeller. The observation of the thrust coefficient is useful because it takes differences in the air density from various measurement sets into account. The measurements show for both fault cases generally lower values than the reference. However, the values vary only by less than 10 %. The impact for medium and high-speed operation is only marginal.

Figure 33 shows the results of the two propeller faults for the generated thrust of the drive train. While there can be a tendency for lower observed thrust for these fault cases, the magnitude is within the range of measurement uncertainty.



**Figure 32. Measured thrust coefficients for propeller faults**



**Figure 33. Thrust for different propeller faults**

Figure 33 also shows the successful simulation of the propeller in the proposed model. For a better clarity of this graph, only the simulation of the reference drive train is shown. The model can also accurately simulate the propeller faults.

### Motor faults

The main motor fault presented in this work is a bearing fault. The fault development was accelerated by applying diamond paste into the bearing. Figure 34 displays the results of this fault case concerning the effective phase current of the motor. Due to an assumed increase of friction and the resulting



torque, there is a general increase of the motor current. Especially, for lower speed this effect is apparent.

The bearing fault simulation was performed by increasing the motor parameter of the static and dynamic friction. For medium and high speed a very good match of the simulated and measured data can be observed. Differences for lower speed can be traced back to stick slip effects during the measurements. This effect could be simulated with non-linear friction coefficients. However, the normal operational speed of the drive train during flight operations is higher than 4500 rpm or 60 % of the maximum thrust. Therefore, the proposed model is sufficient to simulate flight operations under the influence of a bearing fault.

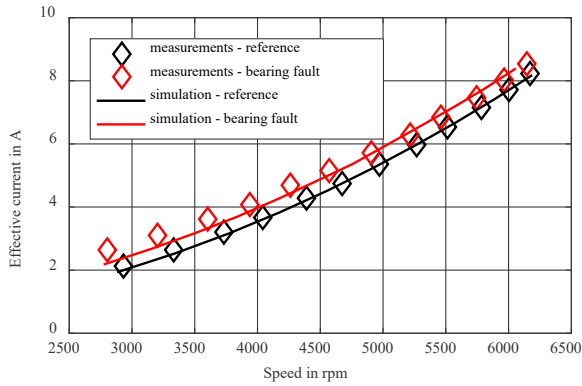


**Figure 34. Effective motor current in case of a bearing fault**

### Efficiency analysis

Figure 35 illustrates the efficiency  $\eta$  of the whole drive train for a reference unit under test and units under test with applied faults.

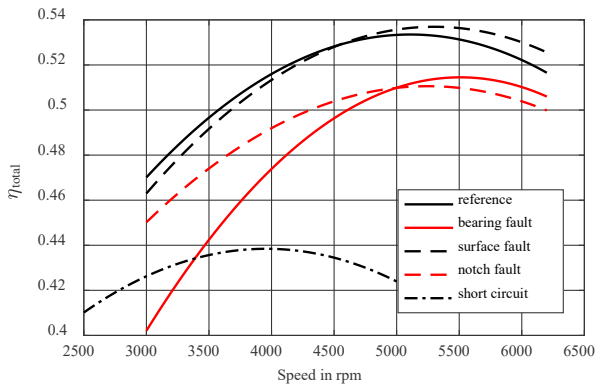


**Figure 35. Determined overall efficiency of applied fault states over the motor speed**

As expected, bearing damage, notch and short-circuit are well below the reference efficiency. Especially the motor with short circuit shows high power losses, which explain the poor efficiency. The losses of the bearing damage can be explained by a higher input power, which is needed to generate the

additional torque due to the higher friction effect. In addition, in this case, much higher engine temperatures are measured. The airscrew error with the roughened surface is remarkable. Here, an improvement in efficiency was found at high speeds. This behavior corresponds to the observations made in [24] on rotor blades of helicopters.

Figure 36 shows the difference in the efficiency of the failures compared to the reference, measured at two positions in the drive train. At position 1 (battery) the efficiency of all cases is identical. Position 2 indicates the combined efficiency of ESC and motor, i. e. the ratio of electrical input power to mechanical shaft power. Position 3 is the propeller efficiency determined from the values of the force sensor. It was assumed that a faulty component could be identified by the different gradients of the efficiency deviations. This also applies very well to the short-circuit and notch fault cases, as well as the bearing fault. As mentioned above, the abrasion of the propeller surface led to an increase in performance, which is the reason that no failure can be identified.

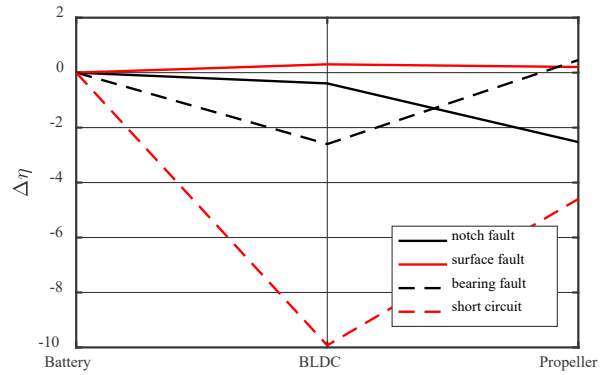


**Figure 36. Partial efficiency difference between fault case and reference at each component of the multicopter drive train**

## 7. INFLUENCE OF FAULTS ON THE FLIGHT PERFORMANCE

The faults applied on the units under test are so serious that it can be assumed that these occur very rarely under normal conditions. In addition, Figure 37 demonstrates that the effects of the fault states on the thrust of the rotor were mostly very small at high motor speeds. The winding short-circuit is an exception. Because thrust losses of about 30% could be observed. However, some fault conditions have resulted in an increase in the power train's input power, which is why the influence on the flight performance values presented in section 2 needs to be discussed. In addition, it could be shown that the efficiency decreases significantly, especially at low speeds. After a failure has occurred, the operating point shifts to higher rotational speeds. In this state not only more energy is required, but also the influence of the coaxial rotors is higher and a faster degradation is expected. All these effects can only be investigated after the complete implementation of the simulation model, which is why only simple

observations with the analytical methods from section 2 can be made.

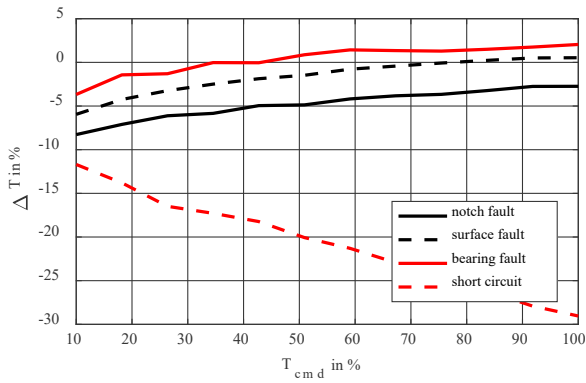


**Figure 37. Thrust differences to reference over commanded thrust**

#### *Hover flight*

The force required for the X8 in hovering flight follows for a single rotor in accordance with equation (1) and (3) to  $T_{h,r}=4.14$  N. With a maximum thrust of  $T_{max}=8.15$  N, this results in a maximum tolerated thrust loss of 49.2 %. Note that the high thrust loss due to the short circuit fault still makes it possible to hover without problems. However, an unfortunate total breakdown of another drive train can lead to an uncontrollable condition. The other faults do not cause any special restrictions.

#### *Axial flight (climb and descent)*

A similar result is obtained for the climb. In the case of a short circuit, the maximum climb rate is reduced to 0.99 m/s, whereas this is nearly unaffected by the other faults. The maximum sink rate is obtained by equation (7) to  $v_{ih} = -v_{zmax} = 5.24$  m/s. As shown above, even in case of a fault,  $v_{ih}$  can still be reached at each rotor. Therefore, none of the failures have an influence on  $-v_{zmax}$ .

#### *Horizontal flight*

The influence of faults on the maximum speed during horizontal flight is even lower. Here  $v_{xmax}$  is reduced from a motor with short circuit only by approx. 1 m/s.

#### *Endurance and range*

The observed efficiency losses are in a range of less than 5%. Assuming that the power requirement for the entire multicopter is 5% higher, the hovering time is reduced by only 20 s. Since the maximum speed is reduced only marginally, it can be assumed that the effects here are rather small.

However, the assumptions should be examined and quantitatively determined in future work with the aid of flight experiments.

## 8. SUMMARY

Unmanned aircraft systems offer numerous applications in a wide range of fields. The multirotor category is strongly represented and the number of multirotor UAVs will increase significantly. In order to enhance flight safety, CM systems offer a wide range of opportunities.

In section 2 the flight mechanics of multicopters were introduced using the X8 with coaxial rotors as an example. Since a consideration of the flight performance parameters of multirotor UAVs is not mentioned very well in the literature, the knowledge in the field of helicopters was used for this work. In the observations on hovering, vertical and horizontal flight, in addition to the take-off mass, it was possible to identify the thrust and its dependence on the induced velocity as the largest influencing factor. Endurance and range are especially dependent on the condition and capacity of the battery. However, the efficiency of the individual drive trains could also be identified as an influencing factor. In addition to the battery, an ESC and a BLDC motor as well as a propeller are involved in the thrust generation of a drive train.

After a detailed presentation of all components, a concept for a CM system was presented. The concept's focus was the evaluation of sensors in terms of their suitability for use with the aid of a specially designed test rig. The concept includes differential pressure sensors to determine the induced speed and thus the propeller thrust, as well as current and voltage measurements to determine the electric power and the motor speed. Small microphones, thermocouples and accelerometers provide additional information for fault detection. In addition to the studies using the test rig, a detailed model of the drive train was developed. Particularly for the engine and operation with a propeller, very good conformity with the measured data was achieved. A further focus of modeling was the calculation of the influence of rotors in coaxial operation. However, the modelling of this effect using BEMT could not adequately explain all effects and overestimates the influence on the generated torque of the lower rotor. The presented simulation environment for validating CM system's algorithms should therefore use data-based description approaches.

Furthermore, the four selected fault conditions of mechanically damaged propellers, abrasion of the propeller, bearing damage in the motor and short circuit in the motor could be described by the model. Through the analyses and validation with measurement data, a deeper understanding of the fault cause was achieved. An investigation of the performance characteristics and efficiencies of the individual components has shown that a CM system is able to record the power losses qualitatively and to identify the faulty component with the help of the applied sensors.

However, the effect of the faults on the flight performance is only minor. An exception is the short circuit, where the high thrust losses play a significant role. Nevertheless, all faults and the condition of the multicopter should be monitored, as a total failure cannot be ruled out in the future.

In further steps, the sensor concept must be integrated into the FSR X8 and evaluated in real flight. In addition, the simulation model used to calculate flight performance must also be evaluated with the aid of flight experiments.

Afterwards, an FDI module can be developed using the simulation model. The information from onboard sensors such as those of the IMU should also be taken into account. Moreover, the effects of various faults on flight performance will be further analyzed. Knowledge of environmental parameters is also important for determining mission-based availability and mission risk. This influences the required flight performance resulting from mission planning, which will be investigated and described in additional studies.

### ACKNOWLEDGEMENTS

The authors would like to thank Mr. Saleh Krüger from the TU Darmstadt as well as Mr. Reinhold Ziegler, Mr. Gerhard-Michael Fresser and Mr. Josef Wildgruber from MBDA Deutschland GmbH for their support and sponsorship of this research work.

### APPENDIX

**Table 3. Copter Data**

Propeller	APC Slow Fly 11x4.7	-
Pitch	4.7 0.11938	inch m
Diameter	11 0.2794	inch m
	11	inch
Motor	Hacker A30-52S	-
ESC	Hacker Pro 20-Opto	-
Flight controller	Pixhawk 4Pro	-
Flow-effective area xy plane $A_{xy}$	0.04	m <sup>2</sup>
Flow-effective area yz plane $A_{yz}$	0.035	m <sup>2</sup>
Copter mass	2.7	kg
Moments of inertia	x axis	0.029
	y axis	0.029
	z axis	0.036
Arm length a	0.424	m

### REFERENCES

- [1] B. Cains, "Unmanned Aircraft Systems (UAS): Commercial Outlook for a New Industry," Washington, USA, Sep. 2015.
- [2] SESAR Joint Undertaking, "European drones outlook study: Unlocking the value for Europe," Belgien, Nov. 2016.
- [3] K. Nonami, F. Kendoul, S. Suzuki, W. Wang, and D. Nakazawa, *Autonomous Flying Robots: Unmanned Aerial Vehicles and Micro Aerial Vehicles*. Tokyo: Springer Japan KK, 2010.
- [4] Office of the Secretary of Defense, "Unmanned Aircraft Systems Roadmap," Washington, USA, Aug. 2005.
- [5] J. Marzat, H. Piet-Lahanier, F. Damongeot, and E. Walter, "Model-based fault diagnosis for aerospace systems: A survey," *Proceedings of the Institution of Mechanical Engineers, Part G: Journal of Aerospace Engineering*, vol. 226, no. 10, pp. 1329–1360, 2011.
- [6] J. C. Monteiro, F. Lizaralde, and Liu Hsu, "Optimal control allocation of quadrotor UAVs subject to actuator constraints," in *2016 American Control Conference (ACC)*, Boston, MA, USA, pp. 500–505.
- [7] D. Wolfram and F. Vogel, "Zustandsüberwachung des Antriebsstrangs kleiner Multikopter zur missionsabhängigen Verfügbarkeitsbestimmung (Condition monitoring of a small multicopter drive train for mission-based availability determination)," TU-Darmstadt Institute of Flight Systems and automatic Control, München, Germany, Sep. 2017.
- [8] J. B. Brandt and M. S. Selig, "Propeller performance data at low reynolds numbers," in *49th AIAA aerospace sciences meeting*, 2011-1255.
- [9] W. Bittner, *Flugmechanik der Hubschrauber (Helicopter Flight Mechanics): Technologie, das flugdynamische System Hubschrauber, Flugstabilitäten, Steuerbarkeit*, 3rd ed. Berlin, Heidelberg: Springer, 2009.
- [10] Wall, Berend Gerdes van der, *Grundlagen der Hubschrauber-Aerodynamik (Fundamentals of helicopter aerodynamics)*. Berlin: Springer Vieweg, 2015.
- [11] E. Torenbeek and H. Wittenberg, *Flight Physics: Essentials of Aeronautical Disciplines and Technology, with Historical Notes*. Dordrecht: Springer Netherlands, 2009.
- [12] C. Molter and P.W. Cheng, "Propeller Performance Calculation for Multicopter Aircraft at Forward Flight Conditions and Validation with Wind Tunnel Measurements," University of Stuttgart, Stuttgart, Germany, 2017.

- [13] M. Podhradsky, J. Bone, C. Coopmans, and A. Jensen, "Battery model-based thrust controller for a small, low cost multirotor Unmanned Aerial Vehicles," in *International Conference on Unmanned Aircraft Systems (ICUAS), 2013: 28 - 31 May 2013, Grand Hyatt Atlanta, Atlanta, Georgia ; conference proceedings*, Atlanta, GA, USA, 2013, pp. 105–113.
- [14] M. Podhradsky, J. Bone, A. Jensen, and C. Coopmans, "Small Low Cost Unmanned Aerial Vehicle Lithium-Polymer Battery Monitoring System," Utah State University, Portland, Oregon, USA, Aug. 2013.
- [15] G. Babel, *Elektrische Antriebe in der Fahrzeugtechnik*, 2nd ed. Wiesbaden: Vieweg+Teubner Verlag / GWV Fachverlage GmbH Wiesbaden, 2009.
- [16] J. C. Gamazo-Real, E. Vázquez-Sánchez, and J. Gómez-Gil, "Position and speed control of brushless DC motors using sensorless techniques and application trends," (eng), *Sensors (Basel, Switzerland)*, vol. 10, no. 7, pp. 6901–6947, 2010.
- [17] Q. Jiang, C. Bi, and S. Lin, "Sensorless control of permanent magnet spindle motors used in hard disk drives," 2005.
- [18] J. Seddon and S. Newman, *Basic helicopter aerodynamics: An account of first principles in the fluid mechanics and flight dynamics of the single rotor helicopter*, 2nd ed. Oxford: Blackwell Science, 2002.
- [19] H. A. Madsen, R. Mikkelsen, S. Øye, C. Bak, and J. Johansen, "A Detailed investigation of the Blade Element Momentum (BEM) model based on analytical and numerical results and proposal for modifications of the BEM model," *J. Phys.: Conf. Ser. (Journal of Physics: Conference Series 75)*, 2007.
- [20] M. McCrink and J. W. Gregory, "Blade Element Momentum Modeling of Low- Re Small UAS Electric Propulsion Systems," in *33rd AIAA Applied Aerodynamics Conference*, Dallas, TX, 2015.
- [21] R. W. Prouty, *Helicopter performance, stability, and control*. Malabar Fla.: Krieger, 2005.
- [22] C. Preusche, C. Anger, and U. Klingauf, "Evaluation of the Training Process of three different Prognostic Approaches based on the Gaussian Process," TU Darmstadt - Institut für Flugsysteme und Regelungstechnik, Nantes Frankreich, Jul. 2014.
- [23] S. Nandi, H. A. Toliyat, and X. Li, "Condition Monitoring and Fault Diagnosis of Electrical Motors—A Review," *IEEE Trans. On Energy Conversion*, vol. 20, no. 4, pp. 719–729, 2005.
- [24] W. N. W. Rohizan, A. S. M. Rafie, M. Y. Harmin, and C. C. Chiang, "Effect of surface roughness on helicopter main rotor blade," *IOP Conf. Ser.: Mater. Sci. Eng.*, vol. 152, p. 12001, 2016.

## BIOGRAPHY



**Daniel Wolfram** received a Diploma (eq. M.Sc.) in Mechanical and Process Engineering from Technische Universität Darmstadt in 2013. Afterwards, he worked at the Institute of Fluid Mechanics and Aerodynamics before he became a research associate at the Institute of Flight Systems and Automatic Control at Technische Universität Darmstadt. In cooperation with MBDA Deutschland GmbH, he works in a project to increase the security of unmanned aerial vehicles by condition-based monitoring.



**Florian Vogel** received a B.Sc. in Mechanical and Process Engineering from Technische Universität Darmstadt, Germany, and from Virginia Polytechnic Institute and State University in 2014. After an internship at Airbus Operations in Hamburg he received his M.Sc. in mechanical engineering at TU Darmstadt in 2017. He wrote his master thesis in the mathematical modelling of small multicopter's powertrains for simulation of selected fault behaviors.



**Dominik Stauder** received a B.Sc. in Mechanical and Process Engineering from Technische Universität Darmstadt, Germany in 2014. Alongside his master's thesis in 2017, he works as a student employee at Lufthansa Aviation Training, where he has been an intern in 2016. He wrote his master thesis in the development of a simulation environment for multicopter's and the implementation of a mathematical model for coaxial rotors.